to be submitted to the Astrophysical Journal

Simulations of JWST images at redshifts z=1—15 using Mid-UV Nearby Galaxy Images from HST

Rogier A. Windhorst

Department of Physics and Astronomy, Arizona State University, Box 871504, Tempe, AZ 85287-1504

Email: Rogier.Windhorst@asu.edu

Chris Conselice

Department of Astronomy, Caltech, MC 105-24, Pasadena, CA 91125

Email: cc@astro.caltech.edu

and Larry Petro

Space Telescope Science Institute, 3700 San Martin Drive, Baltimore, MD 21218

Email: petro@stsci.edu

Keywords: **galaxies: elliptical and lenticular — galaxies: spiral — galaxies: irregular, peculiar — ultraviolet: galaxies — instrumentation: JWST — galaxies: evolution**

ABSTRACT AND CONCLUSIONS

We present realistic simulations of the JWST perfomarmance and present simulated JWST images of galaxies at redshifts z$\simeq$1—15, using as input a systematic imaging survey of 37 nearby galaxies with the Hubble Space Telescope ("HST")/Wide Field and Planetary Camera 2 in the *mid-UV* filter F300W (centered at 2930Å). This local comparison sample is used to simulate what galaxies of a variety of types and star-forming properties at z$\simeq$1–15 would look like to JWST under realistic observing conditions, *if* they existed at these redshifts. At the near-IR wavelengths of JWST, these objects will be observed in their rest-frame far or mid-UV. Any quantitative differences between future real JWST images and the simulations based on our HST mid-UV images can then be used to measure evolutionary effects in galaxy properties. The following are our conclusions:

1) With the planned JWST/NIRCam properties and exposure times of 1.0 hr, galaxies of moderately *high* mid-UV surface brightness [average rest-frame SB(0.29 μm) out to the half-light radius r_e brighter than 23.0 mag arcsec^{-2} at z$\simeq$0] are generally detectable out to z$\simeq$15, although their morphology and SB distribution can generally only be recognized to z$\simeq$7–10.

2) Lower SB extensions [rest-frame SB(0.29 μm) fainter than 23.0 mag arcsec^{-2}] are generally not well visible beyond z$\simeq$5–7 due to the strong $(1+z)^4$ cosmological SB-dimming.

3) Regions of very high SB or star-formation rate, as well as AGN [all with average SB(0.29 μm) out to r_e brighter than 23.0 mag arcsec^{-2}] are generally easily visible to z$\simeq$10–15. For $\lambda \gtrsim 5.3$ μm or z$\gtrsim$15, the JWST InSb QE will drop off rapidly. Hence, should they exist at z$\gtrsim$15, such objects would no longer visible in their rest-frame mid-UV to JWST (of course, they *may* be visible in other rest-frame wavelengths to JWST using other filters or instruments).

4) Objects with high spatial frequency structures are generally recognizable as such to z$\simeq$5–7, beyond which the increasing Θ-z relation and cosmological SB-dimming, as well as the decreasing JWST resolution at longer wavelengths results in reduced resolution and point source sensitivity.

5) High surface brightness mid-UV structures are readily visible and recognizable to z$\simeq$12–15 in very long JWST integrations (>> 10 hrs), *if* JWST is built to meet its *GOALS*. If built to the *minimum REQUIREMENTS*, such objects are visible to z$\simeq$12 in 1-hr exposures, and recognizable only to z$\simeq$7–10. If JWST is built to midway between its *Goals* and *Requirements* (i.e., the *NOMINAL* telescope), then such objects would be visible to z$\simeq$12 at about 2$\times$ lower S/N .

6) The minimum in the Θ-z relation at z$\simeq$1.7 in Λ-dominated cosmologies *and* the JWST diffraction limit at $\lambda \gtrsim 2\mu$m conspire to improve the effective JWST resolution from z$\simeq$2 to z$\simeq$7 for objects of very high mid-UV SB.

1. Introduction

In the early 1990's, ASTRO/UIT imaging was done for about 100 nearby objects in the far-UV (1500Å) and for about 40 objects in the mid-UV (2500Å ; see Bohlin et al. 1992; Hill et al. 1992; Marcum et al. 2001, Kuchinski et al. 2000). This beautiful imaging data set shows that galaxy morphology changes quite dramatically below 3600–4000Å . At these wavelengths, the hot (young) stellar population (mostly in spiral arms and H-II regions) dominates the spectral energy distribution ("SED"), and old red bulges essentially disappear. Thus, galaxies often appear to be of later Hubble type the further one looks into the rest-frame UV. Qualitatively, this is easy to understand. In the optical/near-IR, we see the accumulated luminous phases of long-lived (>1 Gyr) stars, which emit most of their energy at longer wavelengths, whereas the mid-UV samples the star-formation rate ("SFR") averaged over the past Gyr or less, which primarily traces the presently active SF regions, or those regions where star-formation has only recently shut down. The light of high redshift galaxies — which tends to be observed in the rest-frame mid-UV — is dominated by the $\lesssim$1 Gyr populations, and so images in optical pass-bands of high redshift galaxies trace similar stellar population as those observed in the mid-UV in nearby galaxies. Morphological K-corrections derived from UIT and earlier sounding rocket data were first investigated by Bohlin et al. (1991) and Giavalisco et al. (1996).

The mid-UV is the critical wavelength region when comparing the galaxies seen with HST in the I-band at $z \gtrsim 2$ to nearby samples, and to address the question of whether the numerous late-type objects that dominate the faint blue galaxy counts (c.f., Driver et al. 1995a, 1998; Glazebrook et al. 1995; Abraham et al. 1996; Odewahn et al. 1996) are truly new classes of objects, or just reflect the redshifted UV morphology of ordinary galaxies as seen nearby.

A number of authors have explored the effects of band-pass shifting using multicolor optical images (in B and R) to extrapolate to the rest-frame UV on a pixel by pixel basis. This has been done using ground-based data (*e.g.*, Hibbard & Vacca, 1997; Brinchmann et al. 1998) and HST images of galaxies at moderate redshifts (Bouwens, Broadhurst, & Silk 1997; Abraham et al. 1999). These authors conclude that the peculiarities in shape and size distributions found in the deep HST surveys considerably exceed the effects of band-shifting. While this is a robust result, these methods may not capture the full range of rest-frame UV spectral energy distributions in real galaxies, and so are less suitable for making more detailed comparisons with the local universe. There is considerable scatter in the mid-UV for galaxies of a given optical color. For instance, Donas, Milliard & Laget (1995) found a 3 magnitude range in (UV–B) colors at a given (B–R) color in a faint galaxy sample, where a 2000Å filter was used to measure the UV flux. This UV/optical decoupling is also confirmed by the spectroscopy of Treyer et al. (1998). The implication is that the true evolutionary history of galaxies can be very different from that inferred from optical data alone, and that mid–UV observations are necessary for a complete understanding.

Recent observations of the HDF-North with HST/NICMOS have shown that some galaxies differ in their rest-frame UV and optical morphology in samples out to z$\simeq$2.5 (Dickinson et al. al.

2001). Galaxies that appear 'regular' and fit into the Hubble sequence often look very different in rest-frame UV images. As might be expected, these galaxies become more patchy and irregular at shorter wavelengths. However, galaxies with very disturbed morphologies look often very similar in the optical and the UV. These distorted high-z galaxies also have high UV surface brightnesses ("SB") and are forming stars at a high rate. Nearby star-burst galaxies whose structure is dominated by star-formation also have similar morphologies in the rest-frame optical and mid-UV ($e.g.$, Conselice et al. al. 2000, Windhorst et al. 2002), suggesting that these 'peculiar' high-z objects are analogs to nearby star-bursts.

This paper is organized as following. In section 2, we present the WFPC2 sample selection and its processing. In section 3 we briefly discuss the simulation method, and in the Abstract and Figure Captions (of this poster) we discuss the general trends seen in the JWST simulations as a function of SB and redshift. A Λ-dominated cosmology is adopted throughout with a Hubble constant of 71 $km\ s^{-1}\ Mpc^{-1}$ and with Ω_m=0.27, Ω_Λ=0.73.

2. WFPC2 Sample Selection and WFPC2 Observations

In Windhorst et al. (2002), we presented a systematic imaging survey with the HST Wide Field and Planetary Camera 2 ("WFPC2") of 37 nearby galaxies in one or, whenever possible, in two mid-UV bands below the atmospheric cut-off where one can still get reasonable WFPC2 throughput and good red-leak suppression. These filters are F300W (λ_{cent} $\simeq$2930Å ; $\Delta\lambda$ $\simeq$740Å FWHM) and F255W (λ_{cent} $\simeq$2550Å ; $\Delta\lambda$ $\simeq$395Å FWHM). Since the WFPC2 system throughput is about 2.0% in the F300W filter and only about 0.5% in the F255W filter, we expect to detect only the highest SB objects (i.e. the bluest) galaxies in F255W, providing additional constraints to their stellar populations and dust. The mid-UV is the longest wavelength where younger stars can dominate the integrated galaxy light, and therefore an excellent place to measure the SFR averaged over $\lesssim$1 Gyr, and hence provide morphological templates of young star-forming regions that JWST could see at z$\simeq$2–15, if they existed as such at these redshifts.

To match the JWST observations of distant galaxies, the sample consisted of a representative set of all types of nearby galaxies. This includes an emphasis on late-type, Irregular and peculiar galaxies plus compact galaxies and mergers, which are more prevalent at high redshifts (e.g., Driver et al. 1995, 1998). For statistical studies as a function of photometric parameters, we also covered a range in inclination angles: edge-on, face-on, and intermediate angles.

These 37 galaxies were selected for size and surface brightness from several ground-based samples of 725 nearby galaxies in total, as described by Windhorst et al. (2002). From these combined ground-based samples, we selected a subs-ample that covers a wide range of Hubble types and inclinations. The selection criteria for inclusion in the HST/WFPC2 sample are described in detail by Windhorst et al. (2002), and are in short:

(a) Small size: B-band half-light radius in the range $0\farcs1 \lesssim r_{hl} \lesssim 1\farcs0$, as derived from the RC3 catalog (de Vaucouleurs et al. 1991). Hence, about 3–5 scale-lengths fit in a single WFPC2 frame, thus avoiding the need to mosaic the objects with multiple WFPC2 fields.

(b) High predicted average surface brightness in F300W out to the half-light radius $r_{hl} = r_e$: $18 \lesssim$ SB(F300W) $\lesssim$ 22.5–23.0 mag arcsec^{-2} . The average SB in F300W was predicted from the total B-magnitudes, B_T, the (U–B) color measurements from aperture photometry, and the r_{hl} values, as tabulated in the RC3. The bias towards selecting higher SB galaxies can be addressed as in Driver et al. (1995b). In short, selecting high SB galaxies as the nearby template objects is not an important issue when comparing them to high redshift galaxies, since the high redshift samples are also similarly biased in favor of high SB galaxies due to the strong cosmological SB-dimming, where the light dims monochromatically as $(1 + z)^{(4+\alpha)}$. Here, α is the spectral index if the object spectrum were to be represented by a power-law SED (which is approximately correct for a young flat SED in the UV).

2.1. WFCP2 Processing and Red-leak Corrections

The standard WFPC2 processing contained optimal bias and dark-subtraction plus flat-fielding, which was done as in Windhorst et al. (1994b, 1994c, 1998a), Driver et al. (1995a), and Odewahn et al. (1996). Calibration was done with the STSDAS On-The-Fly ("OTF") routines available since summer 2000. The F300W filter has a significant red-leak, as described quantitatively in chapter 3 of the WFPC2 Handbook (*cf.* Biretta et al. 2000). This results in a fraction of the object's red flux (longwards of 4000Å) that leaks into the F300W filter. In short, for making red-leak corrections, it is sufficient to subtract 5–7% of the F814W image from the F300W image for stellar populations dominated by K3V–K4V stars, and never more than 10% for an old stellar population dominated by K8V stars.

3. Simulation Method

The JWST simulations were done following the method of Giavalisco et al. (1996), who simulated the appearance of nearby galaxies seen with ASTRO/UIT at 1500–2500Å to HST at redshifts z$\simeq$2–3. In essence, they argued that they need to dim the observed monochromatic SB as $\propto(1+z)^5$, but with one factor of (1+z) dropping out because the calculations as done in terms of CCD ADU, while another factor of (1+z) is largely mitigated in their case, because the filters in which the high redshift objects are observed are correspondingly wider. So they resample the UV images as expected from the Θ-z relation, and use an effective SB-dimming $\propto(1+z)^3$. Since we will not be able make our filters arbitrarily wide (i.e. wider than $\Delta\lambda/\lambda$=100%) for our much higher redshift JWST objects, we will conservatively adopt a SB-dimming $\propto(1+z)^4$, while using a maximum filter width of $\Delta\lambda/\lambda$=0.5 (i.e. Res=2) that does not fully compensate for the fourth $(1+z)^4$ term.

Fig. 1 shows the angular size vs. redshift relation for our Lambda dominated cosmology. Note that the in the top panel, the relation is linear in 1/z for z$\lesssim$0.05 (the small angle approximation) and nearly linear in z for z$\gtrsim$3 (the Lambda dominated universe). Hence, all curvature occurs in the range 0.05$\lesssim$z$\lesssim$3, which is coded up for the JWST simulations.

Fig. 2 shows the adopted JWST throughput curves for a single gold reflection. All 9 mirrors in the JWST OTE and ISIM mirrors are coated with gold for optimal reflectivity at wavelengths $\gtrsim$0.6μm. The transmission for the quartz dewar window and the filters are assumed to be 95%. The observations are simulated for the JWST NIR Camera ("NIRCam"), which has an InSb detector. Its QE curve shows rapid cutoffs for $\lambda\gtrsim$5.3 μm and for $\lambda\lesssim$0.6μm. Other details of the simulations are given in the captions of Figures 4.01–4.06. In short, the InSb detector read-noise and dark current are set at the *NOMINAL* **values of 4.4e^- and 0.0044e^- /sec, respectively, although Fig. 4.06b and 4.06c show the** *BEST CASE*, **if JWST is built to meet its** *GOALS* **(RN=1.5e^- and Dark=0.0022e^- /sec; including a 100-hr exposure!), and the** *WORST CASE,* **if JWST only meets its** *REQUIREMENTS* **(RN=7.0e^- and Dark=0.050e^- /sec). Unless otherwise indicated, all exposures are 1.0 hr, and to reduce effects from CR's, the noise is simulated for read-outs every 900 sec. The JWST PSF was approximated as a Gaussian. Note in Fig. 4.01–4.06 that JWST does not become diffaction limited until $\lambda\gtrsim$2μm (so for all $\lambda\lesssim$2μm the 6-meter FWHM=0$''$.084).**

Fig. 3. shows the adopted JWST background at the Ecliptic Pole as seen from JWST's location in the L2 point. These were calculated following the JWST Mission Simulator (NMS) of Petro (2001). Contributions from the Zodiacal and Thermal background are shown separately. The background clearly increases for $\lambda\gtrsim$3.5 μm, which is visible in the simulations in Fig. 4.01–4.06. The JWST background used was normalized to an H-band surface brightness of 21.7 mag arcsec^{-2} in the Vega system, which is approximately consistent with the darkest on-orbit V-band surface brightness seen at the NEP with HST/WFPC2 (V=23.2 mag arcsec^{-2} , Windhorst et al. 1998), and the V–H color of the Sun of 1.44 mag.

All the above wavelengths dependent relations were fit with segmented smooth polynomials as plotted by the dashed lines in Fig. 1–3. Further details on the JWST simulations can be found in our IRAF script, which together with all simulated JWST images will be made public via: www.public.asu.edu/afs/asu.edu/clas/iraf/www/HST_UBAND/data/JWSTsims/

4. Acknowledgements

RAW, CC, and LP acknowledge support from the Space Telescope Science Institute (RAW through grants GO-8645 and GO-9124), which is operated by the Association of Universities for Research in Astronomy, Inc., for NASA under contract NAS 5-26555. RAW thanks Pete Stockman and the JWST group at STScI for their hospitality and help during a working visit in summer 2001 when which much of this work was done. We thank John Hibbard for helpful discussions.

REFERENCES

Abraham, R. G., Tanvir, N.R., Santiago, B. X., Ellis, R.S., Glazebrook, K., van den Bergh, S. 1996, MNRAS, 279, L47

Abraham, R. G., et al. 1999, MNRAS, 308, 569

Bohlin, R. C., et al. 1991, ApJ, 368, 12

Bouwens, R. J., Broadhurst, T., & Silk, J. 1998, ApJ, 506, 579

Bruzual A., G. & Charlot, S. 1993, ApJ, 405, 538

Burg, C. A., Windhorst, R. A., Odewahn, S. C., de Jong, R. S., & Frogel, J. A. 1997, in "The Ultraviolet Universe at Low and High Redshift: Probing the Progress of Galaxy Evolution", ed. W. H. Waller, M. N. Fanelli, J. E. Hollis, & A. C. Danks (New York: AIP Press), Vol. 408, 434

Conselice, C. J., Gallagher, J. S., Calzetti, D., Homeier, N., & Kinney, A. 2000, AJ, 119, 79

Cornett, R. H., et al. 1994, ApJ, 426, 553

de Jong, R. S. 1996b, A&A, 313, 45; — 1996c, A&A, 313, 377

de Vaucouleurs, G., de Vaucouleurs, A., Corwin, H., Buta, R., Paturel, G., & Fouqué, P. 1991, Third Reference Catalogue of Bright Galaxies (New York: Springer Verlag)

Dickinson, M. E. 2001, "Building Galaxies: From the Primordial Universe to the Present," proceedings of the XIXth Moriond Astrophysics Meeting (March 1999), ed. F. Hammer, et al. (Paris: Ed. Frontieres), 257

Driver, S., Fernandez-Soto, A., Couch, W., Odewahn, S., Windhorst, R., et al. Phillipps, S., Lanzetta, K., & Yahil, A. 1998, ApJL, 496, L093

Driver, S. P., Windhorst, R. A., Ostrander, E. J., Keel, W. C., Griffiths, R. E., & Ratnatunga, K. U. 1995a, ApJL, 449, L023

Driver, S. P., Windhorst, R. A., & Griffiths, R. E. 1995b, ApJ, 453, 48

Ellis, R.S., Colless, M., Broadhurst, T., Heyl, J., & Glazebrook, K. 1996, MNRAS, 280, 235

Eskridge, P. B., Frogel, J. A., de Grijs, R., Gallagher, J. S., Matthews, L. D., O'Connell, R. W., Taylor, V. A., Odewahn, S. C., & Windhorst, R. A. 2002, ApJL, submitted

Giavalisco, M., Livio, M., Bohlin, R. C., Macchetto, F. D., & Stecher, T. P. 1996, AJ, 112, 369

Glazebrook, K., Ellis, R. E. Santiago, B. & Griffiths, R. E. 1995, MNRAS, 275, L19

Hibbard, J. E. & Mihos, J. C. 1995, AJ, 110, 140

Hibbard, J. E., & Vacca, W. D. 1997, AJ, 114, 1741

Keel, W. C., & Windhorst, R. A. 1993, AJ, 106, 455

Kuchinski, L. E., et al. 2000, ApJS, 131, 441 (astro-ph/0002111)

Kuchinski, L. E., Madore, B. F., Freedman, W. L., & Trewhella, M. 2001, ApJ, in press (astro-ph/0106454)

Marcum, P. M., et al. 2001, ApJS, 132, 129

Odewahn, S. C., Windhorst, R. A., Driver, S. P., & Keel 1996, ApJL, 472, L013

Odewahn, S. C., Burstein, D., & Windhorst, R. A. 1997, AJ, 114, 2219

Petro, L. 2001, the Next Generation Space Telescope Simulator NMS, STScI, www.ngst.stsci.edu/nms/main/nms_flux_form.html

Williams, R.E., et al. 1996, AJ, 112, 1335

Windhorst, R. A., Franklin, B. E., & Neuschaefer, L. W. 1994a, PASP, 106, 798

Windhorst, R. A., Keel, W. C., & Pascarelle, S. M. 1998, ApJL, 494, L27

Windhorst, R., et al. 1998b, in Proceedings of the STScI Symposium on "The Hubble Deep Field", ed. M. Livio, S. M. Fall, & P. Madau (Cambridge University Press), 481

Windhorst, R. A., Taylor, V. A., Odewahn, S. C., Chiarenza, C. A., de Grijs, R., de Jong, R. S., Frogel, J. A., Eskridge, P. B., Gallagher, J. S., Conselice, C., Hibbard, J., Matthews, L., MacKenty, J., & O'Connell, R. W. 2002, ApJS, in press.

This preprint was prepared with the AAS LaTeX macros v5.0.

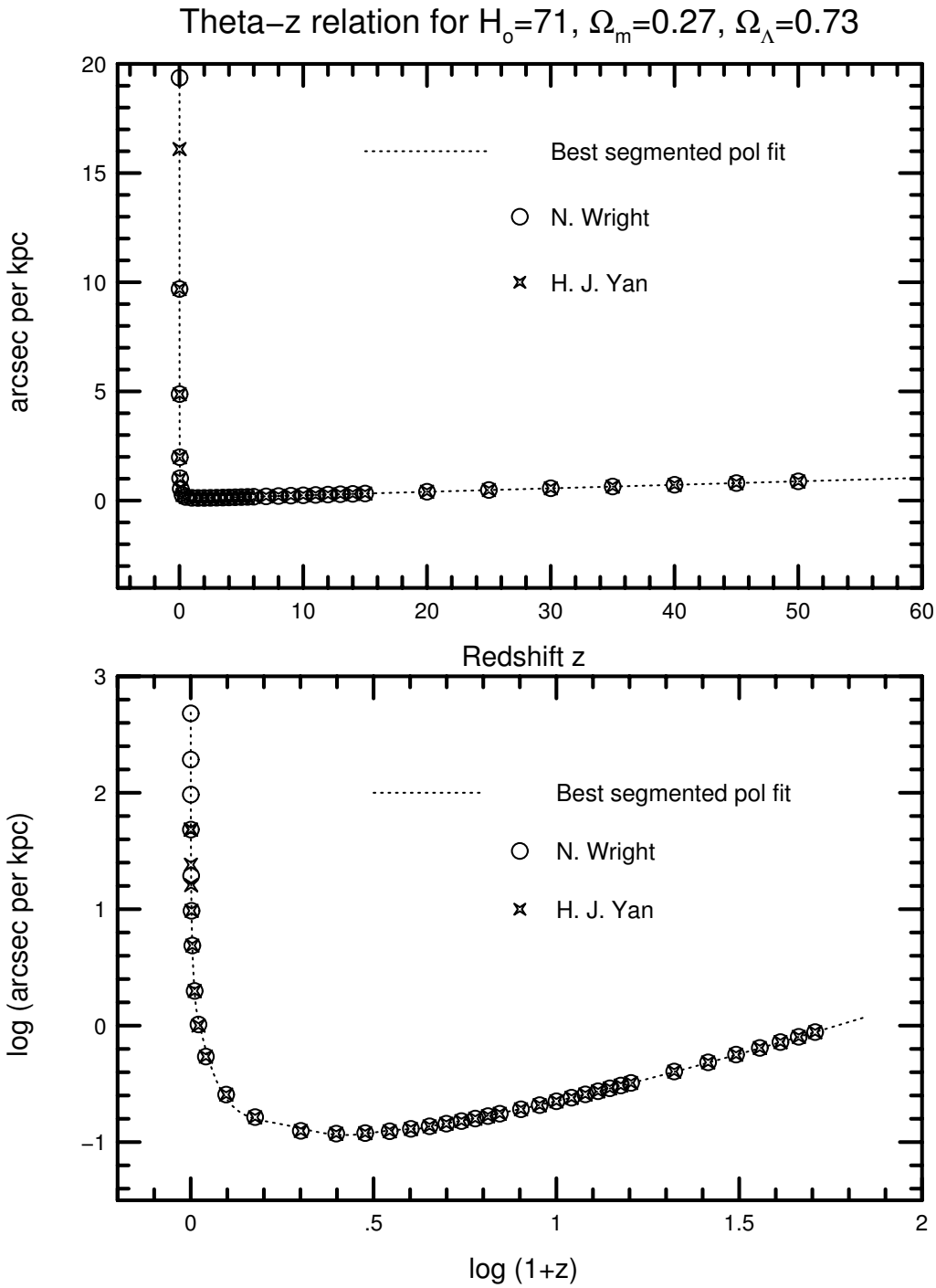

Fig. 1. Angular size vs. redshift relation in a Lambda dominated cosmology of H_0 =71 $km\ s^{-1}\ Mpc^{-1}$, Ω_m=0.27, Ω_Λ=0.73. Note that the in the top panel, the relation is nearly linear in 1/z for z$\lesssim$0.05 (the small angle approximation) and linear in z for z$\gtrsim$3 (the Lambda dominated universe). All curvature occurs in the range 0.05$\lesssim$z$\lesssim$3, which is coded up in the IRAF script that does the JWST simulations.

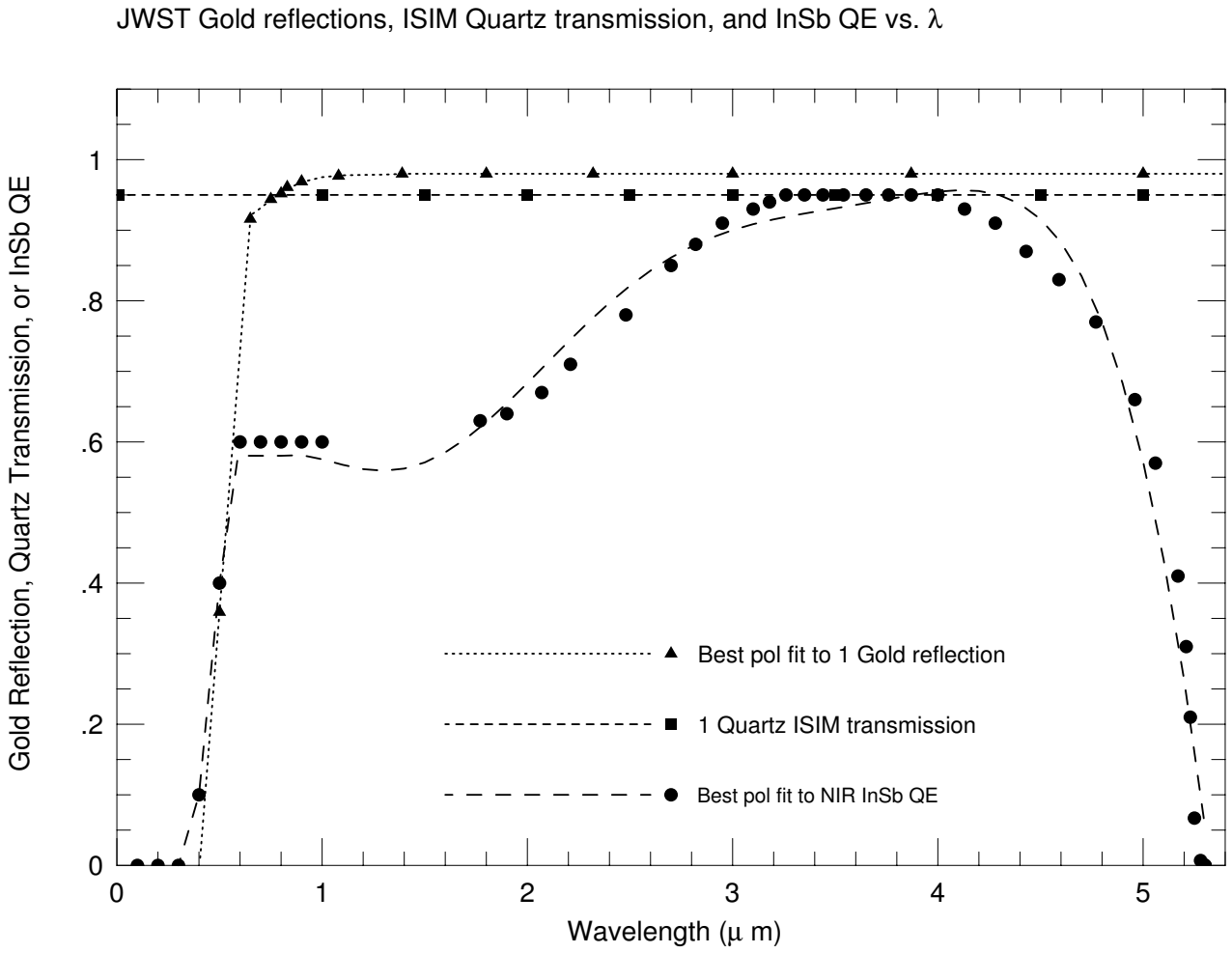

Fig. 2. The adopted JWST throughput curves for gold reflections in the OTA and ISIM mirrors (9 mirrors in total – the relation shown here is for one reflection), for the quartz dewar window and filter transmission (both are assumed to be =0.95), and for the NIR InSb QE. Note that the INSb QE curve shows rapid cutoff's for $\lambda \gtrsim 5.3$ μm and for $\lambda \lesssim 0.6\mu$m. All relations were fit with segmented polynomials as plotted by the dashed lines, and coded up accordingly in the IRAF script that does the JWST simulations.

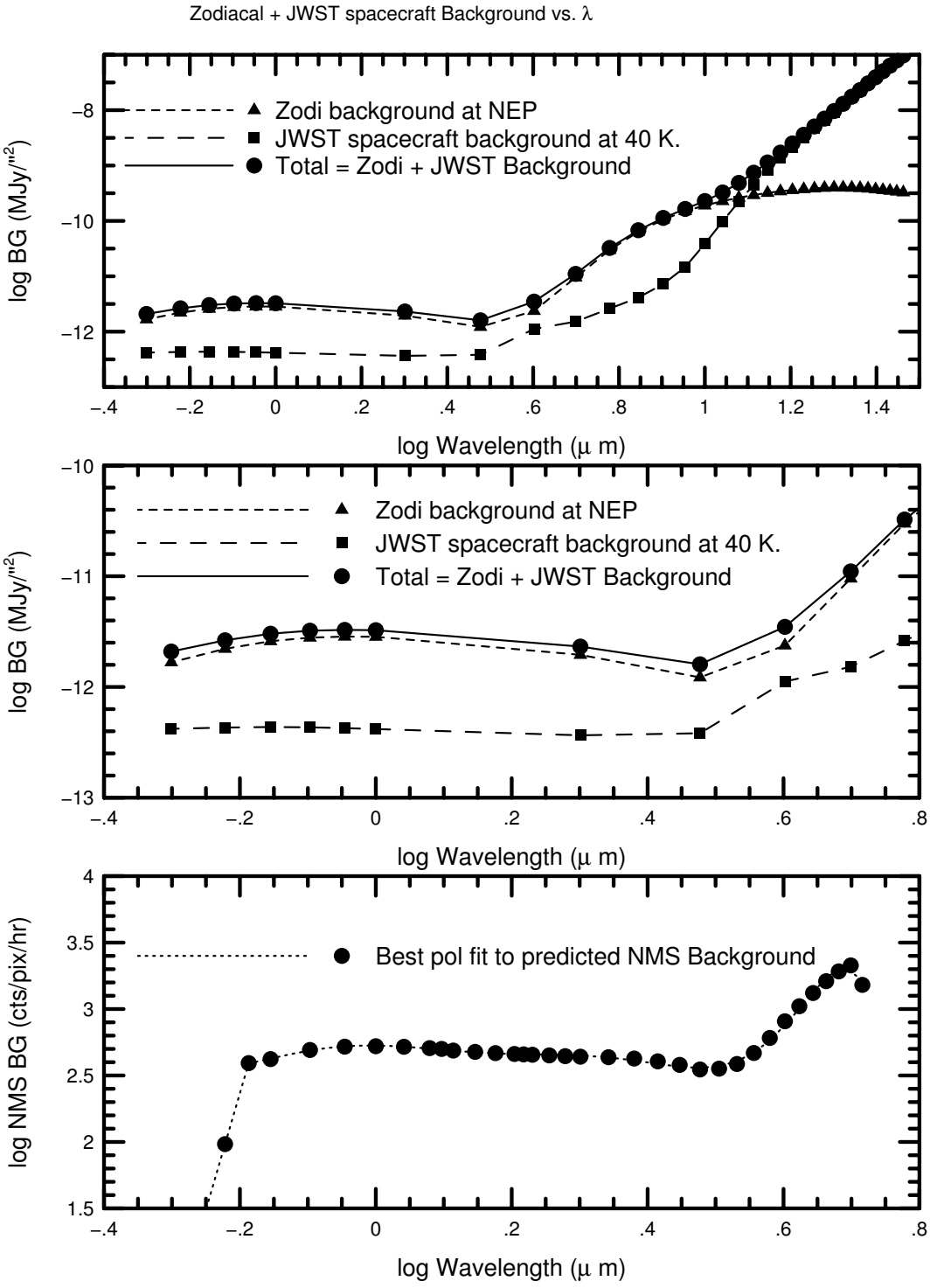

Fig. 3. The adopted JWST background at the NEP as seen from L2. Contributions from the Zodi and Thermal background are shown separately. The background clearly increases for $\lambda \gtrsim 3.5$ μm, which is visible in the simulations in Fig. 4.nn. These relations were fit with segmented polynomial as plotted by the dashed lines, and coded up accordingly in the IRAF script that does the JWST simulations.

The JWST background used was normalized to an H-band surface brightness of 21.7 mag arcsec^{-2} in the Vega system, which is approximately consistent with the darkest on-orbit V-band surface brightness seen in the NEP with HST/WFPC2 (V=23.2 mag arcsec^{-2} , Windhorst et al. 1998), and the V–H color of the Sun of 1.44 mag.

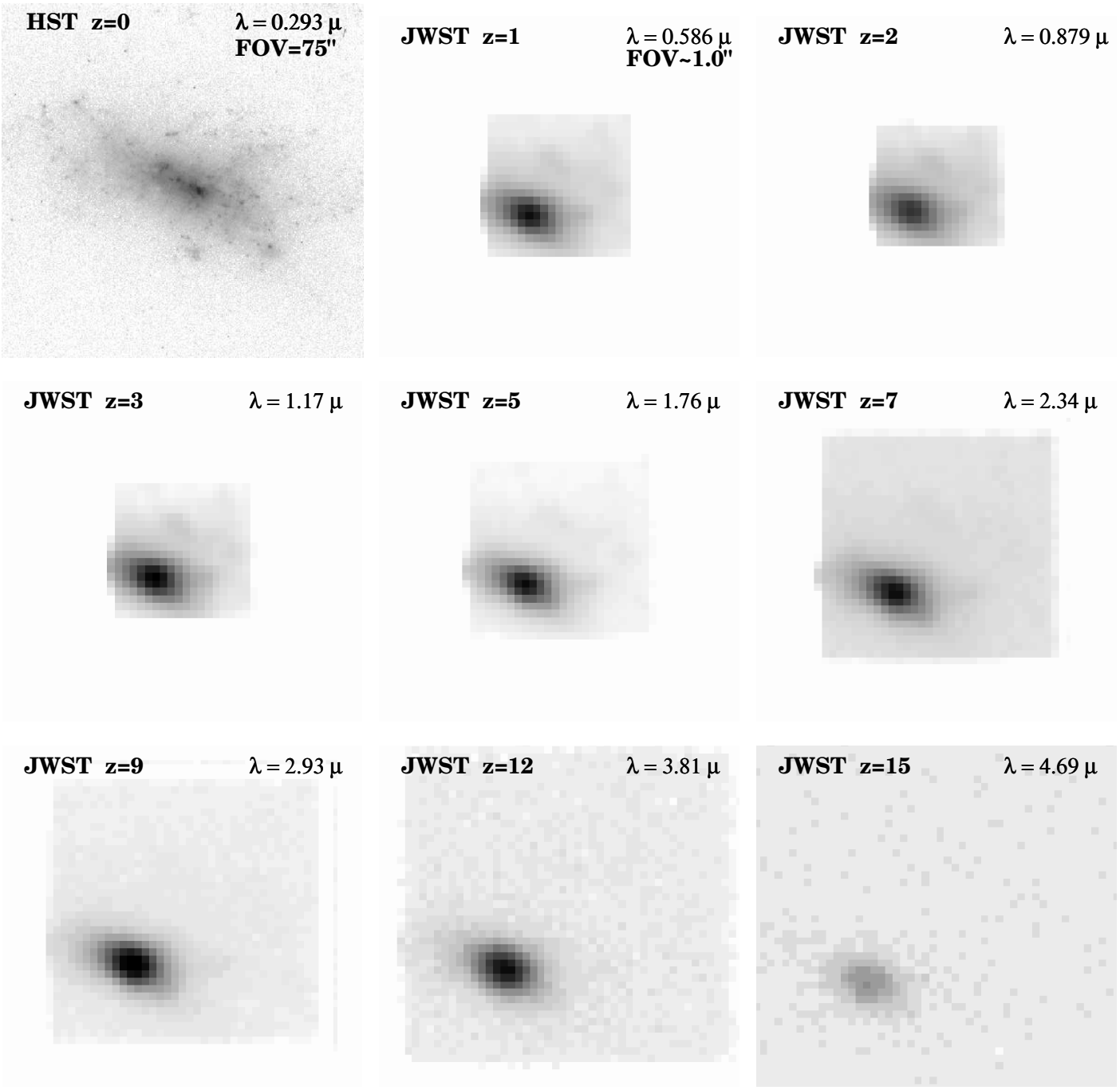

Fig. 4.01. JWST simulations based on HST/WFPC2 F300W images of the dwarf irregular NGC1140 (z=0.0050). This compact high SB object would be visible to z≃15, but hard to classify at all z≥1.

ASSUMPTIONS: COSMOLOGY: H_0=71 km/s/Mpc, Ω_m=0.27, and Ω_Λ=0.73.

INSTRUMENT: 6.0 m effective aperture, JWST/NIRCam, 0.034″ /pix, RN=5.0 e^-, Dark=0.020 e^-/sec, NEP H-band Sky=21.7 mag/arcsec^2 in L2, Zodiacal spectrum, t_{exp}=1.0 hrs, read-out every 900 sec.

Row 1: z=0.0 (HST λ=0.293μm, FWHM=0.04″), z=1.0 (JWST λ=0.586μm, FWHM=0.084″), and z=2.0 (JWST λ=0.879μm, FWHM=0.084″).

Row 2: z=3.0 (JWST λ=1.17μm, FWHM=0.084″), z=5.0 (JWST λ=1.76μm, FWHM=0.084″), and z=7.0 (JWST λ=2.34μm, FWHM=0.098″).

Row 3: z=9.0 (JWST λ=2.93μm, FWHM=0.122″), z=12.0 (JWST λ=3.81μm, FWHM=0.160″), and z=15.0 (JWST λ=4.69μm, FWHM=0.197″)

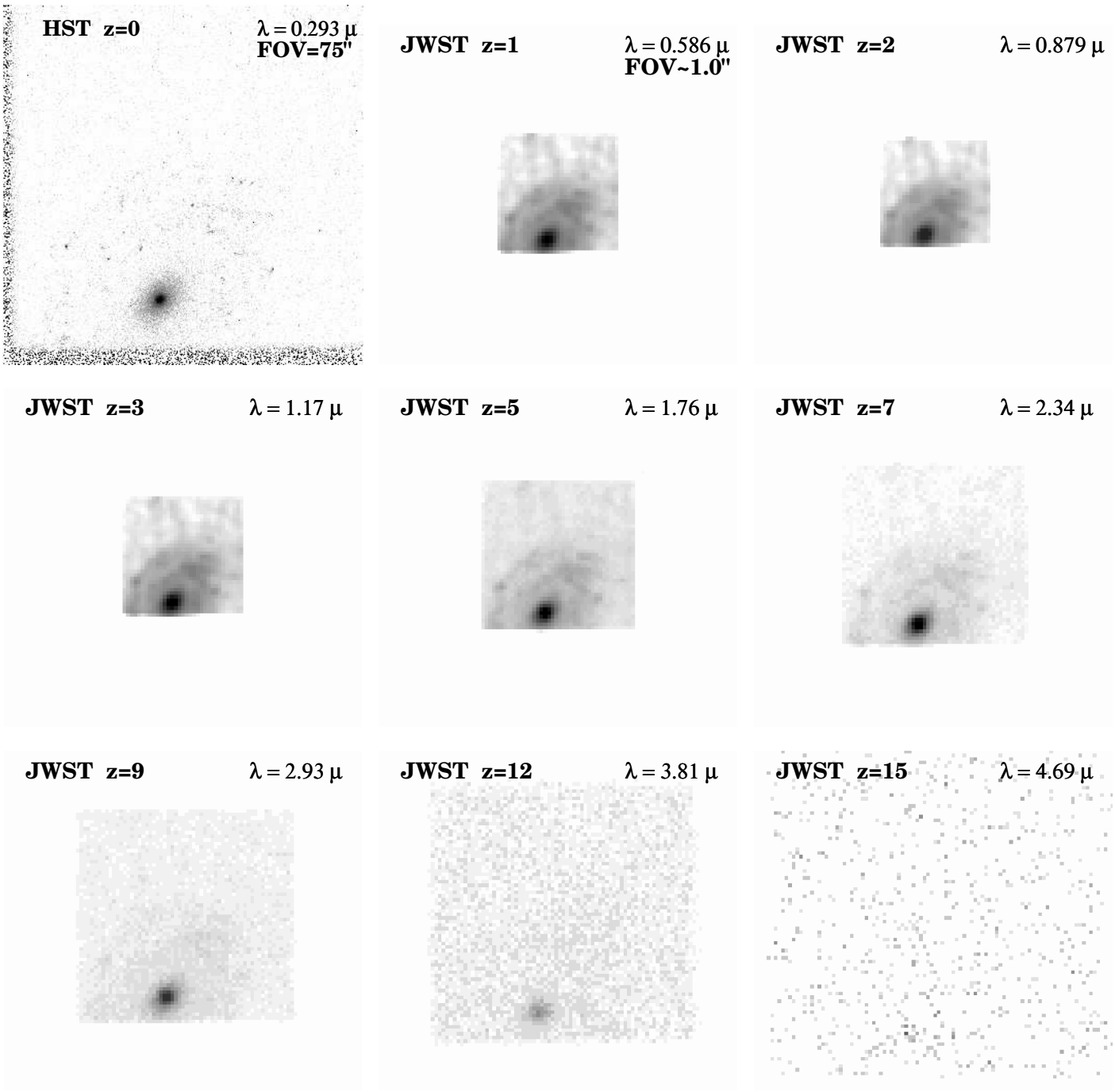

Fig. 4.02. JWST simulations based on HST/WFPC2 F300W images of the mid-type spiral NGC2551 (0.0078). Such an object would be visible to z≃10, but only recognizable to z≃7.

ASSUMPTIONS: COSMOLOGY: H_0=71 km/s/Mpc, Ω_m=0.27, and Ω_Λ=0.73.

INSTRUMENT: 6.0 m effective aperture, JWST/NIRCam, 0.034″ /pix, RN=5.0 e^-, Dark=0.020 e^-/sec, NEP H-band Sky=21.7 mag/arcsec^2 in L2, Zodiacal spectrum, t_{exp}=1.0 hrs, read-out every 900 sec.

Row 1: z=0.0 (HST λ=0.293μm, FWHM=0.04″), z=1.0 (JWST λ=0.586μm, FWHM=0.084″), and z=2.0 (JWST λ=0.879μm, FWHM=0.084″).

Row 2: z=3.0 (JWST λ=1.17μm, FWHM=0.084″), z=5.0 (JWST λ=1.76μm, FWHM=0.084″), and z=7.0 (JWST λ=2.34μm, FWHM=0.098″).

Row 3: z=9.0 (JWST λ=2.93μm, FWHM=0.122″), z=12.0 (JWST λ=3.81μm, FWHM=0.160″), and z=15.0 (JWST λ=4.69μm, FWHM=0.197″)

FOV=75"

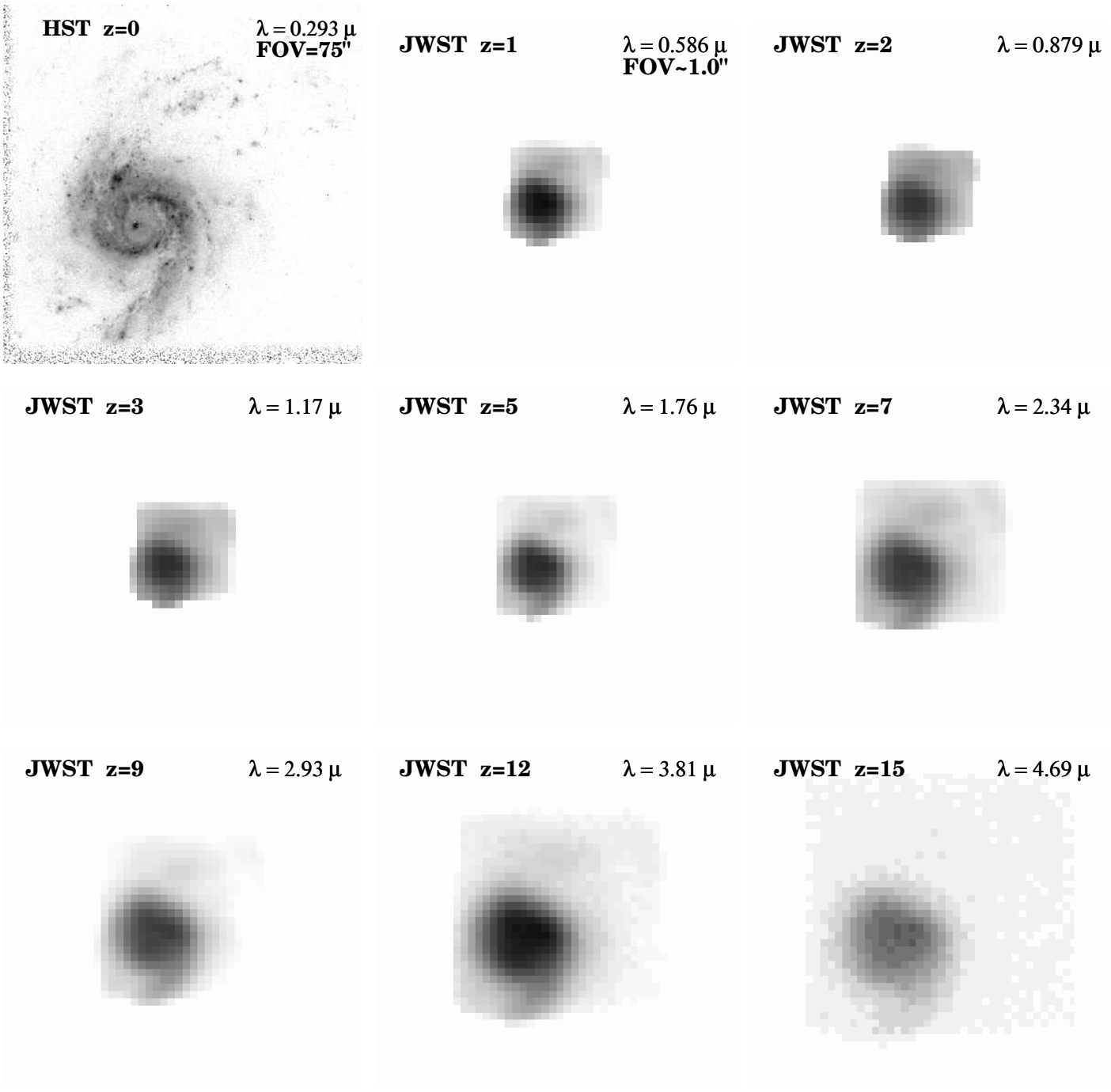

Fig. 4.03. JWST simulations based on HST/WFPC2 F300W images of the high-SB starbursting dwarf spiral galaxy NGC3310 (0.0033). The minimum in the Θ-z relation at z$\simeq$1.7 and the JWST diffraction limit at $\lambda \geq$2.2μm — combined with the object's very high rest-frame UV SB — conspire to improve the effective JWST resolution on the mid-UV morphology of this object from z$\simeq$2 to z$\simeq$7.

ASSUMPTIONS: COSMOLOGY: H_0=71 km/s/Mpc, Ω_m=0.27, and Ω_Λ=0.73. INSTRUMENT: 6.0 m effective aperture, JWST/NIRCam, 0.034″ /pix, RN=5.0 e^-, Dark=0.020 e^-/sec, NEP H-band Sky=21.7 mag/arcsec^2 in L2, Zodiacal spectrum, t_{exp}=1.0 hrs, read-out every 900 sec.

Row 1: z=0.0 (HST λ=0.293μm, FWHM=0.04″), z=1.0 (JWST λ=0.586μm, FWHM=0.084″), and z=2.0 (JWST λ=0.879μm, FWHM=0.084″). **Row 2:** z=3.0 (JWST λ=1.17μm, FWHM=0.084″), z=5.0 (JWST λ=1.76μm, FWHM=0.084″), and z=7.0 (JWST λ=2.34μm, FWHM=0.098″). **Row 3:** z=9.0 (JWST λ=2.93μm, FWHM=0.122″), z=12.0 (JWST λ=3.81μm, FWHM=0.160″), and z=15.0 (JWST λ=4.69μm, FWHM=0.197″)

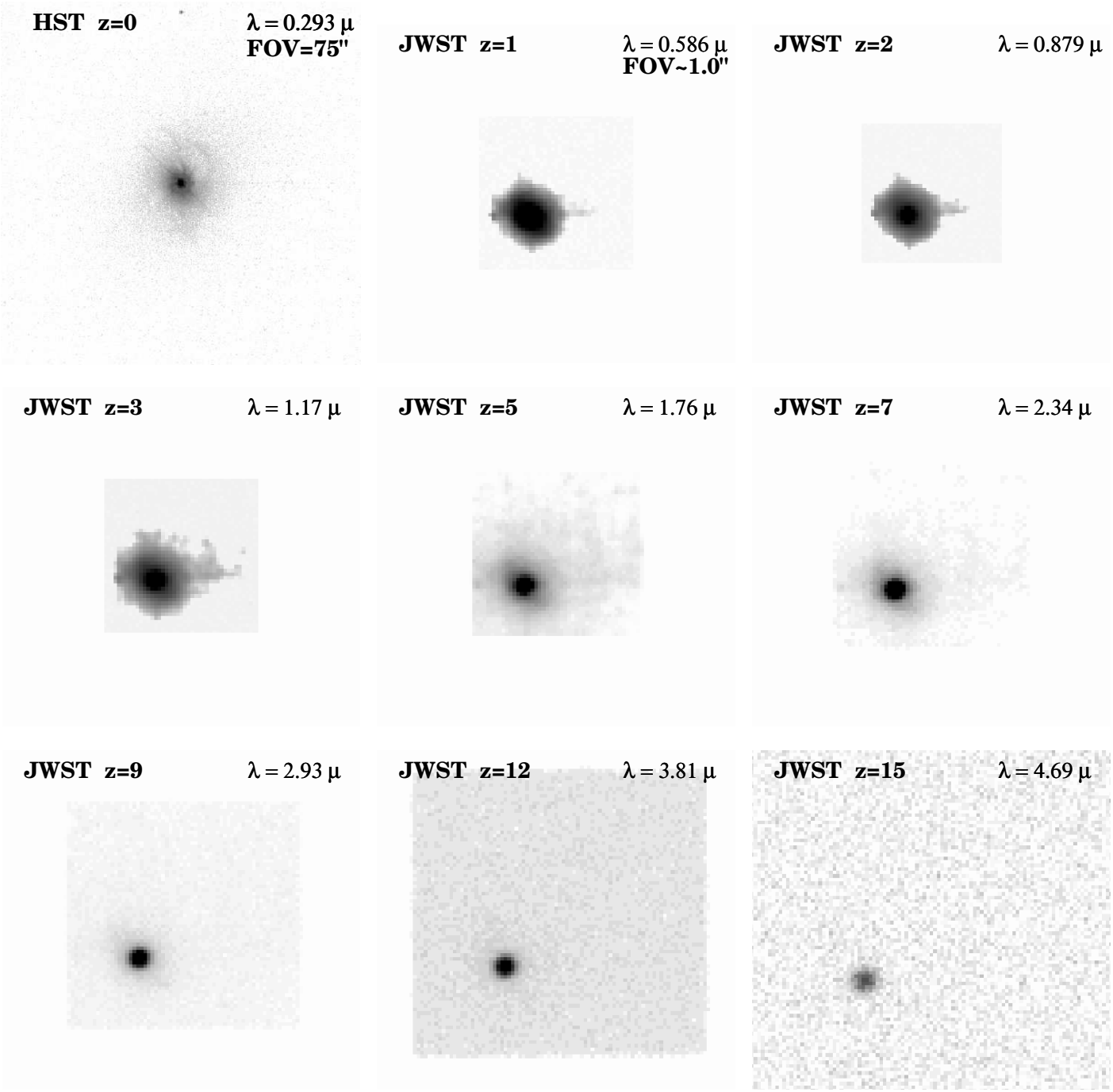

Fig. 4.04. JWST simulations based on HST/WFPC2 F300W images of the Seyfert galaxy NGC3516 (0.0088). Note that the faint nebulosity surrounding the AGN in the mid-UV at z=0 essentially disappears at z$\geq$7, so that at high redshifts such objects would look like a pure AGN.

ASSUMPTIONS: COSMOLOGY: H_0=71 km/s/Mpc, Ω_m=0.27, and Ω_Λ=0.73.

INSTRUMENT: 6.0 m effective aperture, JWST/NIRCam, 0.034″ /pix, RN=5.0 e^-, Dark=0.020 e^-/sec, NEP H-band Sky=21.7 mag/arcsec^2 in L2, Zodiacal spectrum, t_{exp}=1.0 hrs, read-out every 900 sec.

Row 1: z=0.0 (HST λ=0.293μm, FWHM=0.04″), z=1.0 (JWST λ=0.586μm, FWHM=0.084″), and z=2.0 (JWST λ=0.879μm, FWHM=0.084″). **Row 2:** z=3.0 (JWST λ=1.17μm, FWHM=0.084″), z=5.0 (JWST λ=1.76μm, FWHM=0.084″), and z=7.0 (JWST λ=2.34μm, FWHM=0.098″). **Row 3:** z=9.0 (JWST λ=2.93μm, FWHM=0.122″), z=12.0 (JWST λ=3.81μm, FWHM=0.160″), and z=15.0 (JWST λ=4.69μm, FWHM=0.197″)

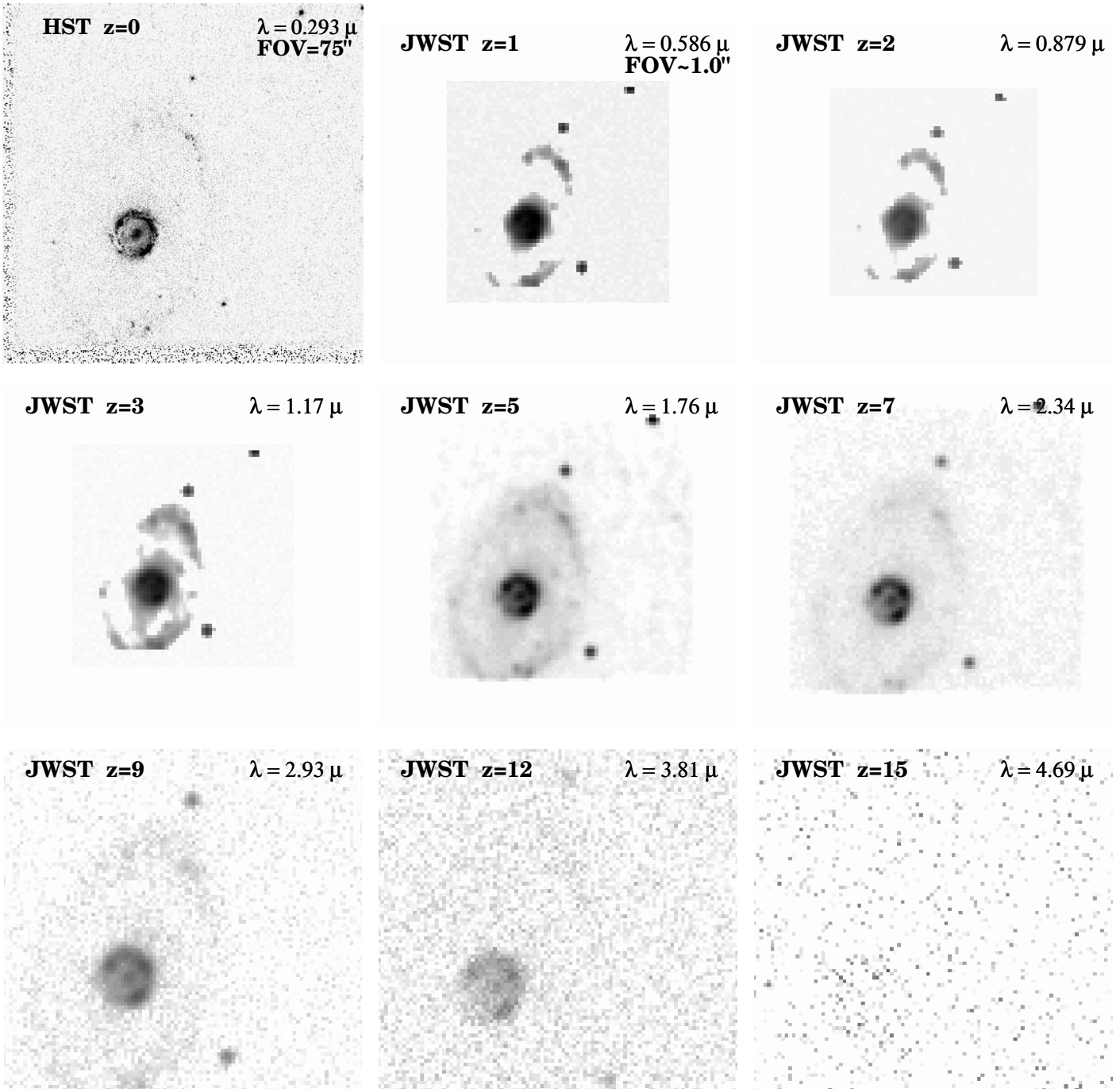

Fig. 4.05. JWST simulations based on HST/WFPC2 F300W images of the barred ring galaxy NGC6782 (0.0125). Note again that for z≃2–7, the effective resolution on the bright star-forming ring improves with increasing redshift, until the $(1+z)^4$-dimming completely kills it for z≥10.

ASSUMPTIONS: COSMOLOGY: H_0=71 km/s/Mpc, Ω_m=0.27, and Ω_Λ=0.73.

INSTRUMENT: 6.0 m effective aperture, JWST/NIRCam, 0.034″ /pix, RN=5.0 e^-, Dark=0.020 e^-/sec, NEP H-band Sky=21.7 mag/arcsec^2 in L2, Zodiacal spectrum, t_{exp}=1.0 hrs, read-out every 900 sec.

Row 1: z=0.0 (HST λ=0.293μm, FWHM=0.04″), z=1.0 (JWST λ=0.586μm, FWHM=0.084″), and z=2.0 (JWST λ=0.879μm, FWHM=0.084″). **Row 2:** z=3.0 (JWST λ=1.17μm, FWHM=0.084″), z=5.0 (JWST λ=1.76μm, FWHM=0.084″), and z=7.0 (JWST λ=2.34μm, FWHM=0.098″). **Row 3:** z=9.0 (JWST λ=2.93μm, FWHM=0.122″), z=12.0 (JWST λ=3.81μm, FWHM=0.160″), and z=15.0 (JWST λ=4.69μm, FWHM=0.197″)

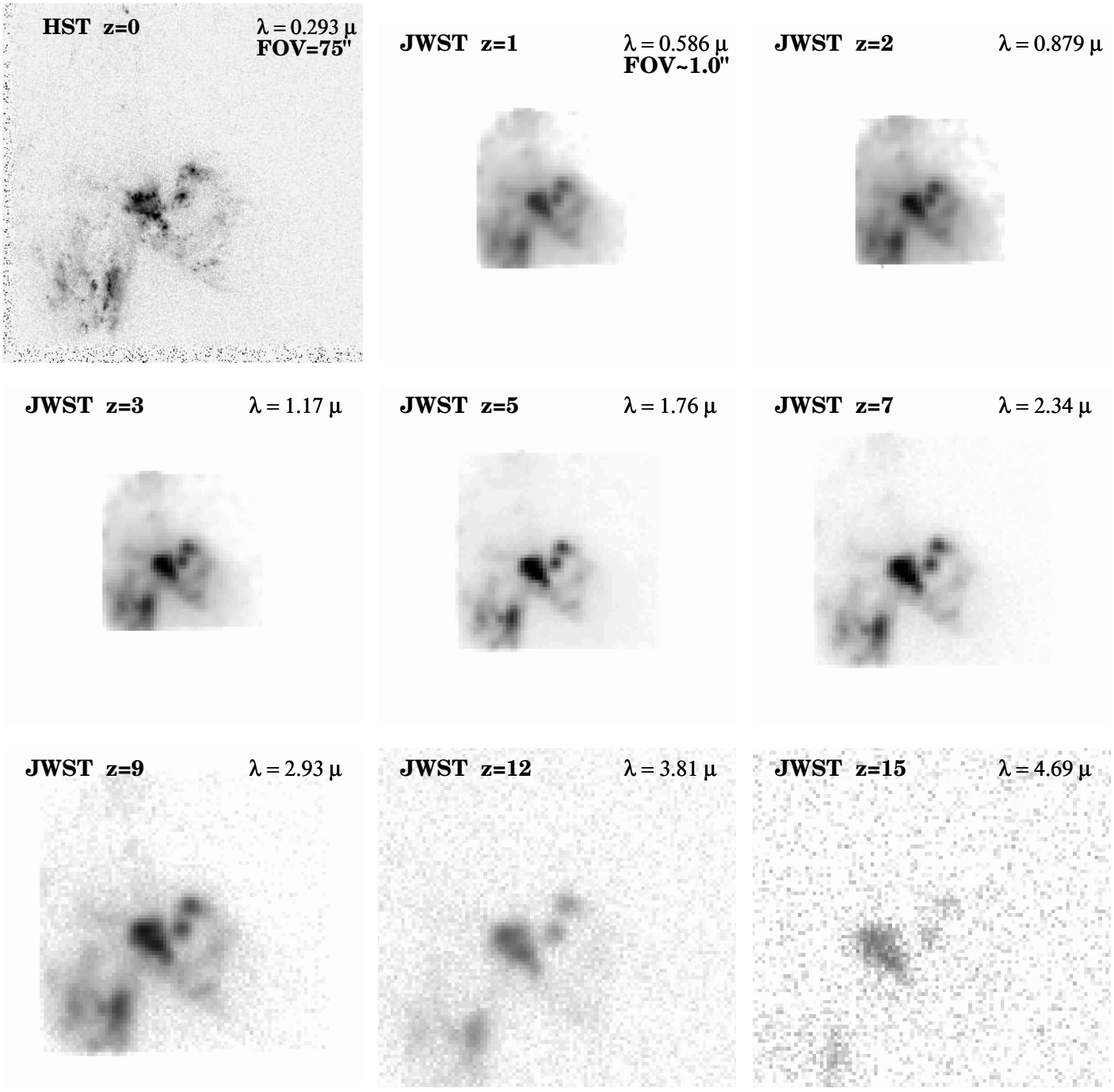

Fig. 4.06.a. JWST simulations based on HST/WFPC2 F300W images of the merger UGC06471-2 (z=0.0104). Note that the two unresolved star-bursting knots in the center remain visible until z∼12, beyond which the SB-dimming also kills their flux. This is the NOMINAL JWST [= (GOALS+REQUIREMENTS)/2].

ASSUMPTIONS: COSMOLOGY: H_0=71 km/s/Mpc, Ω_m=0.27, and Ω_Λ=0.73.

INSTRUMENT: 6.0 m effective aperture, JWST/NIRCam, 0.034″ /pix, RN=5.0 e^-, Dark=0.020 e^-/sec, NEP H-band Sky=21.7 mag/arcsec^2 in L2, Zodiacal spectrum, t_{exp}=1.0 hrs, read-out every 900 sec ("NOMINAL").

Row 1: z=0.0 (HST λ=0.293μm, FWHM=0.04″), z=1.0 (JWST λ=0.586μm, FWHM=0.084″), and z=2.0 (JWST λ=0.879μm, FWHM=0.084″). **Row 2:** z=3.0 (JWST λ=1.17μm, FWHM=0.084″), z=5.0 (JWST λ=1.76μm, FWHM=0.084″), and z=7.0 (JWST λ=2.34μm, FWHM=0.098″). **Row 3:** z=9.0 (JWST λ=2.93μm, FWHM=0.122″), z=12.0 (JWST λ=3.81μm, FWHM=0.160″), and z=15.0 (JWST λ=4.69μm, FWHM=0.197″)

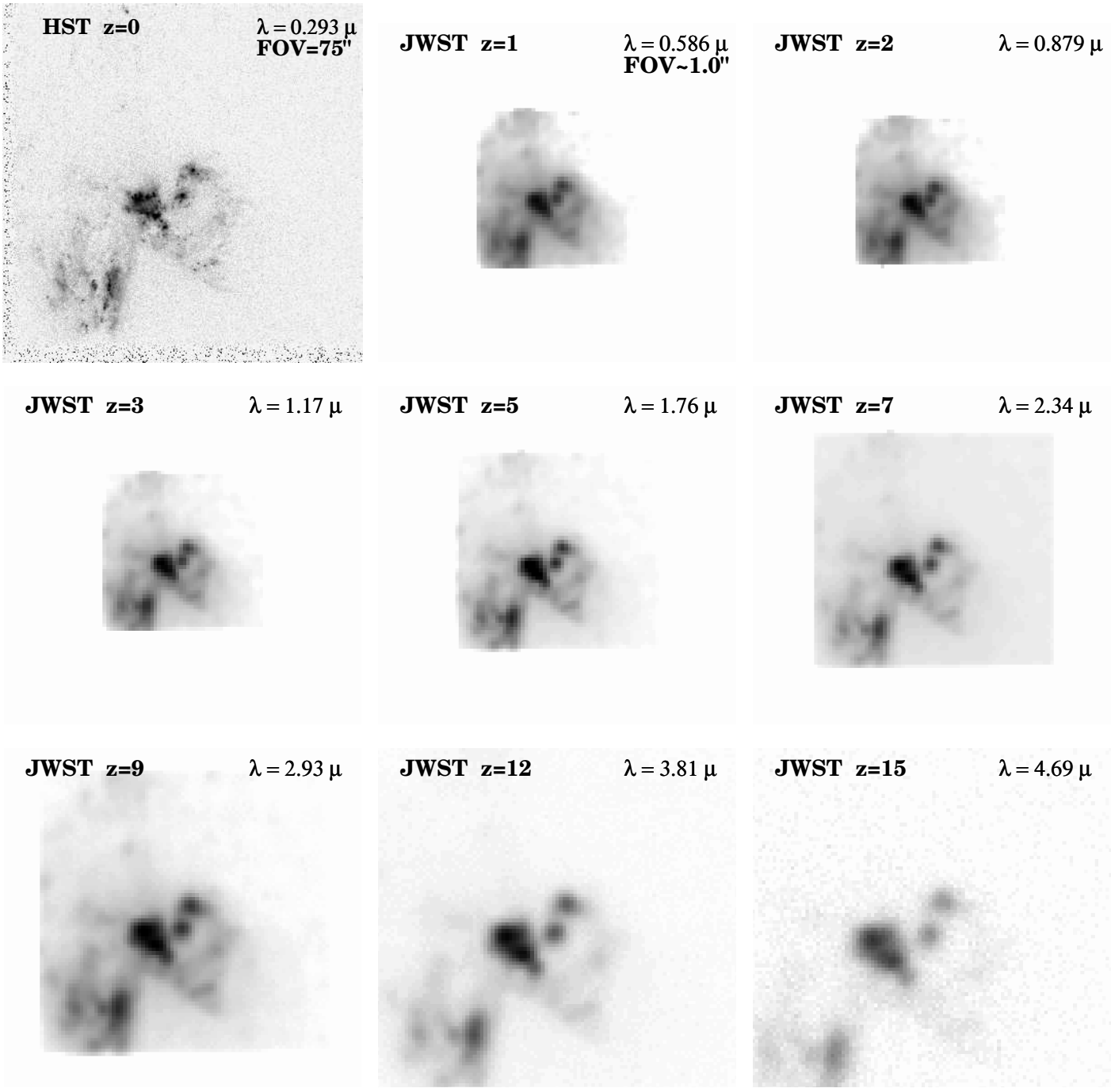

Fig. 4.06.c. JWST simulations based on HST/WFPC2 F300W images of the merger UGC06471-2 (z=0.0104). This is the BEST CASE JWST [meeting all GOALS, and t_{exp}=100 hrs]. The object is recognizable to z≃15.

ASSUMPTIONS: COSMOLOGY: H_0=71 km/s/Mpc, Ω_m=0.27, and Ω_Λ=0.73.

INSTRUMENT: 6.0 m effective aperture, JWST/NIR camera, 0.034″ /pix, RN=3.0 e^-, Dark=0.010 e^-/sec, NEP H-band Sky=21.7 mag/arcsec^2 in L2, Zodi spectrum, t_{exp}=100.0 hrs, read-out every 900 sec ("GOALS").

Row 1: z=0.0 (HST λ=0.293μm, FWHM=0.04″), z=1.0 (JWST λ=0.586μm, FWHM=0.084″), and z=2.0 (JWST λ=0.879μm, FWHM=0.084″). **Row 2:** z=3.0 (JWST λ=1.17μm, FWHM=0.084″), z=5.0 (JWST λ=1.76μm, FWHM=0.084″), and z=7.0 (JWST λ=2.34μm, FWHM=0.098″). **Row 3:** z=9.0 (JWST λ=2.93μm, FWHM=0.122″), z=12.0 (JWST λ=3.81μm, FWHM=0.160″), and z=15.0 (JWST λ=4.69μm, FWHM=0.197″)